IEEE Access
Multidisciplinary | Rapid Review | Open Access Journal

Received November 23, 2019, accepted December 14, 2019, date of publication December 24, 2019,
date of current version January 8, 2020.

Digital Object Identifier 10.1109/ACCESS.2019.2962078

Dual-Wideband High-Gain Fabry-Perot Cavity Antenna

YAN-HE LV, (Student Member, IEEE), XIAO DING, (Member, IEEE), AND BING-ZHONG WANG, (Senior Member, IEEE)
Institute of Applied Physics, University of Electronic Science and Technology of China, Chengdu 610054, China

Corresponding author: Bing-Zhong Wang (bzwang@uestc.edu.cn)

This work was supported in part by the National Natural Science Foundation of China under Grant 61731005, in part by the National Natural Science Foundation of China under Grant 61901086, in part by the Aeronautical Science Foundation of China under Grant ASFC-20162080008, in part by the Postdoctoral Innovation Talents Support Program under Grant BX20180057, in part by the China Postdoctoral Science Foundation under Grant 2018M640907, in part by the Fundamental Research Funds for the Central Universities under Grant ZYGX2019J101, and in part by the Opening Project of Guangxi College Key Laboratory of Microwave and Optical Wave Applications Technology.

ABSTRACT In this paper, we proposed a novel Fabry-Perot cavity antenna with high-gain radiation over two wide bands based on a partially reflective metasurface. To satisfy the resonance condition of the dual-wideband Fabry-Perot cavity, we constructed the unit cell of the partial reflection metasurface by loading magnetic coupling enhancement layers and etching the bottom patches. The partial reflection metasurface composed of the above unit cells can generate reflection phases of positive gradient with almost the same slope over two wide bands, where the partial reflection amplitude is close to 1. Subsequently, a normal dual-band microstrip antenna has also been designed for excitation. Finally, the Fabry-Perot cavity antenna consists of the proposed partial reflection metasurface and the dual-band antenna has been simulated, fabricated, and measured in a microwave anechoic chamber. Both simulation and experimental results demonstrate that the designed Fabry-Perot cavity antenna achieves 3-dB gain bandwidths of 20.7% and 10.1% with peak gains of 12.07dBi and 13.5dBi over two wide bands of 5.7-6.9GHz and 11.7-12.95GHz, respectively.

INDEX TERMS Fabry-Perot cavity antenna, metasurface, partially reflective surface, dual band, wideband.

I. INTRODUCTION

High gain radiation from a finite aperture is a long-standing technical discussion in the field of electromagnetism [1]–[4]. Fabry-Perot cavity antenna (FPCA) is a simple and efficient choice for achieving high gain radiation [5], which is widely applied in the frontier fields including long-range wireless communications [6], [7], high directional data transmission [8], efficient energy transfer [9] and fifth-generation (5G) wireless communication [10]. Normally, a conventional FPCA consists of a partially reflective surface (PRS), a metal ground on the bottom layer, and an antenna as a source in the cavity. The radiation is reflected back and forth between the PRS and the metal ground of the cavity. When a part of the radiation wave reaches the outside of the cavity, it generates an in-phase superposition that effectively increases the antenna directivity along the boresight significantly. Therefore, the ideal operating conditions for a high-gain FPCA can be summarized as [4]

$$\phi_H + \phi_L = \frac{4\pi f}{c}h + 2N\pi, N = 1, 2, 3, \ldots \quad (1)$$

where f is the operating frequency and h is the cavity height. ϕ_H and ϕ_L represent the reflection phases of the PRS and the ground plane of the cavity, respectively. According to (1), when the reflection phase ϕ_L and the height h are fixed, the PRS reflection phase ϕ_H of an ideal high-gain FPCA needs to increase with the operating frequency f. For most conventional FPCAs, since the phase curve of ϕ_H has a negative slope, high gain radiation is limited to a narrow band. Therefore, the reflection phase of the PRS having a positive gradient is significant for breaking the operating bandwidth limit of a high-gain FPCA.

As analyzed above, broadband operating has always been the focus of FPCA researches [14]–[16]. In [14], T. S. Bird's group originally proposed a PRS composed of dipole-strip

The associate editor coordinating the review of this manuscript and approving it for publication was Lin Peng.

unit cells. The novel PRS they proposed can achieve the positive gradient reflection phase, which can effectively extend the gain bandwidth of the FPCA. Based on the above method, an FPCA with a multi-layer PRS is proposed for broadband operating [15]. The multi-layer PRS forms three cavities in the FPCA, which generates the positive gradient reflection phase and increases the 3-dB gain bandwidth to 15%. In [16], Y. J. Guo's group designed a four-layer PRS for both dual polarization and high-gain radiation over a wide band. In addition to wideband operation, the multi-band characteristics of FPCA are also limited by (1). An ideal multi-band FPCA requires the reflection phase of the PRS to satisfy (1) at multiple frequencies. In [17], a partially reflective metasurface (PRMS) composed of anisotropic MS (Metasurface) unit cells was proposed to realize a dual-band FPCA. The designed FPCA achieves the high-gain radiation at 8.75 GHz and 9.8 GHz for TE and TM polarizations, respectively. However, the radiation patterns have different shapes and different polarizations over the two frequency bands, and the 3dB gain bandwidths are only 2.5% and 6.1%, respectively. In [18], S. Gao's group developed a dual-layer FSS for a triband high-gain FPCA. The dual-layer FSS generates three FP (Fabry-Perot) cavities at different resonant frequencies. Similarly, the multi-frequency design of a dual-layer FSS still has only a narrow operating band around each frequency point. For practical applications, multi-band FPCA with wideband high-gain radiation has more research prospects. According to (1), an ideal multi-wideband FPCA requires the positive gradient reflection phase ϕ_H over each operating band and maintains their slope the same. In [19], M. L. Abdelghani's group developed a dual-band WLAN antenna with a dual-layer PRS. The dual-layer PRS with an air interlayer forms two resonant cavities, which broaden the 3-dB gain bandwidth of the higher band to 11%. However, the 3-dB gain bandwidth of the lower band is only 7% around the 2.5GHz. In recent works, multiple cavities (multilayer PRS with air barriers) seems to be a necessary technical means for multi-band FPCA. However, this design significantly increased the profile height and fabricating difficulty, which masks the conventional engineering application advantages of FPCA.

Inspired by previous excellent works, we innovatively proposed a dual-wideband high-gain FPCA based on a novel PRMS. The designed PRMS consists of isotropic MS unit cells, which are optimized by loading magnetic coupling enhancement layers and specific etching. The PRMS unit cell exhibits the positive gradient reflection phases with quasi-identical slope over two wide bands of 5.5-6.5 GHz and 11.5-12.5 GHz, where partial reflection amplitude remains above 0.7. Under the excitation of a dual-band microstrip antenna, the designed FPCA widens the 3dB gain bandwidths to 20.7% and 10.1% with peak gains of 12.07dBi and 13.5dBi over two wide bands of 5.7-6.9GHz and 11.7-12.95GHz, respectively. The main innovations of this paper include:

i. Proposing a PRMS unit cell that implements a reflection phase ϕ_H of positive gradient and quasi-identical slope over two wide bands.

ii. Satisfying FP resonance condition over two wide bands with a single FP cavity.

iii. Designing, processing, and measuring a novel FPCA that achieves high-gain radiation over two wide bands.

II. PRMS DESIGN STRATEGY FOR DUAL-WIDEBAND FPCA

A. OPERTION PRINCIPLE

As mentioned above, a PRMS without the air interlayer is designed for high-gain radiation over two wide bands. In other words, we employ only one cavity to satisfy the required reflection phase conditions in (1) over two wide bands. According to (1), the slope k_d of the reflection phase curve $\phi_H - f$ of an ideal FPCA can be expressed as follows:

$$k_d = \frac{\phi_H + \phi_L - 2N\pi}{f} = \frac{4\pi}{c}h, \quad N = 0, 1, 2, \ldots \tag{2}$$

For the structure of a conventional FPCA, the bottom reflection phase ϕ_L and the cavity height h are fixed. Therefore, the PRMS of a dual-wideband FPCA not only has a positive gradient reflection phase ϕ_H over two wide bands, but also the slopes k_1 and k_2 of its reflection phase curve $\phi_H - f$ should satisfy the following conditions on these two wide bands:

$$k_d = k_1 - k_2 > 0 \tag{3}$$

In addition, the broadside directivity D of an ideal FPCA can be expressed as a function of the reflection coefficient $|\Gamma|$ of the PRS [14]:

$$D = 10 \cdot \log(\frac{1 + |\Gamma|}{1 - |\Gamma|}) \tag{4}$$

Thus, in order to achieve a dual-band FPCA, the reflection coefficient $|\Gamma|$ of the desired PRMS should be as close as possible to 1 in both two wide bands. To satisfy the above (3) and (4), we design and optimize the PRMS unit cell according to the following steps:

a) PRMS unit cell with positive gradient reflection phase over a wide band
b) PRMS unit cell with positive gradient reflection phase over two wide bands
c) PRMS unit cell with positive gradient reflection phase over two wide bands with almost the same slopes, which maintains the FP resonance condition on both wide bands.

B. DESIGN OF UNIT CELL WITH POSITIVE GRADIENT REFLECTION PHASE

Based on the above discussion, a unit cell with the positive gradient reflection phase over a wide band is proposed, which is called unit cell A in the subsequent description. Unit cell A consists of a top square patch, a bottom cross patch, and a middle substrate (ε_{r1} =2.2 and $\tan\delta$ =0.0009) with a thickness of 1mm, as shown in Figs. 1(a), (b) and (c). This type of PRS unit cell has also been employed for a beam-steerable FPCA, which is derived from the wide adjustable

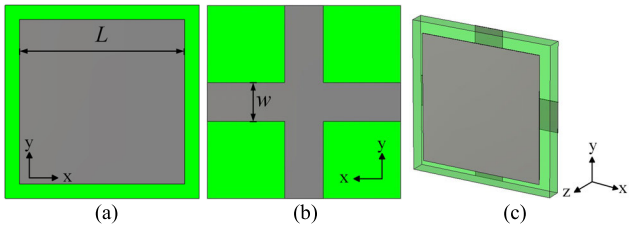

FIGURE 1. Schematic of a unit cell A with the positive gradient reflection phase over a single wide band, (a) a front view, (b) a back view, and (c) a 3D view.

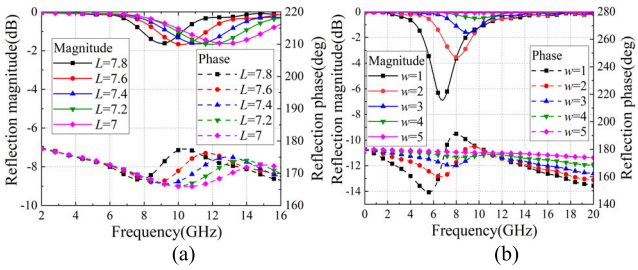

FIGURE 2. Reflection magnitude and reflection phase of a unit cell A. (a) width of the cross patch w is 3mm, and length of the square patch L changes from 7mm to 7.8mm. (b) length of the square patch L is 7.6mm, and width of the cross patch w changes from 1mm to 5mm.

range of the reflection phase of such unit cells [20]. By means of the commercial software CST, the reflection coefficient of unit cell A is simulated under the illumination of the x-polarized plane wave in the $+z$ direction, as shown in Figs. 2(a) and (b). In Fig. 2(a), as the length L increases from 7 to 7.8 mm, the positive gradient reflection phase of unit cell A has a higher frequency band position, a larger bandwidth, and a smaller slope. However, the reflection amplitude can be maintained at a high level regardless of the change of L. In Fig. 2(b), as the width w increases from 1 to 5 mm, the bandwidth of the positive gradient reflection phase increases, and the slope becomes smaller. However, the reflection amplitude becomes lower as the width w reduces.

In Figs. 2(a) and (b), the unit cell A obtains a positive gradient reflection phase whose position and bandwidth can be separately controlled by adjusting the length L and the width w. Furthermore, it can be observed that the reflection amplitude produces a depression in the band of the positive gradient reflection phase.

C. DESIGN of UNIT CELL WITH DUAL-BAND POSITIVE GRADIENT REFLECTION PHASE

In order to analyze the mechanism of the positive gradient reflection phase, a unit cell A with $L = 7.6$mm and $w = 3$mm is simulated for the electric field distribution at 10 GHz. In Figs. 3(a) and (b), when unit cell A generates a positive gradient reflection phase, there is a significant resonance around the square patch with the polarization of the incoming wave. Therefore, we slot the top square patch as unit cell B to obtain homogeneous resonances with different electrical lengths, which can produce positive gradient reflection phases over two different bands, as shown

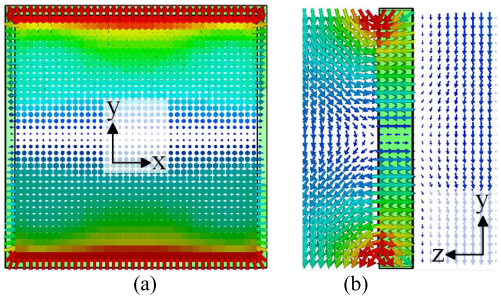

FIGURE 3. The (a) front view and (b) side view of electric field distribution of the unit cell A with w =3mm, L =7.6mm at the f =10GHz.

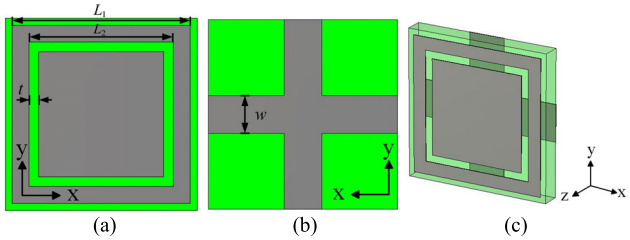

FIGURE 4. Schematic of a unit cell B with positive gradient reflection phase over two wide bands, (a) a front view, (b) a back view, and (c) a 3D view.

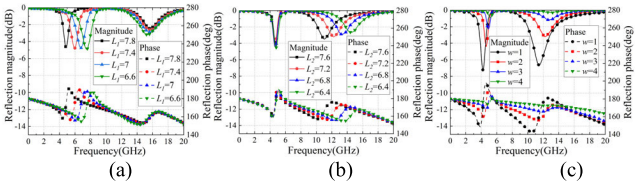

FIGURE 5. Reflection magnitude and reflection phase of unit cell B. (a) t =0.4 mm, w =2 mm, L_2 = 6 mm, and L_1 varies from 7 to 7.8 mm, (b) t =0.4 mm, w =2 mm, L_1 = 7.8 mm, and L_2 varies from 6.4 to 7.6 mm, (c) t =0.4 mm, L_1 = 7.8 mm, L_2 = 7.2 mm, and w varies from 1 to 4 mm.

in Figs. 4(a), (b) and (c). A similar structure has also been applied to IoT devices with two narrow operating bands [22] Under the same conditions and excitation, a unit cell B with varying structural parameters is simulated for reflection phase and magnitude over two bands, as shown in Figs. 5(a), (b), and (c). Regardless of the change in parameters L_1, L_2, or w, the unit cell B generates a positive gradient reflection phase over two wide bands. In Fig. 5(a), when L_1 varies from 7 to 7.8 mm, the positive gradient reflection phase of lower band moves towards the low-frequency region, but that of the higher band is not affected. In Fig. 5(b), when L_2 varies from 6.4 to 7.6 mm, the positive gradient reflection phase of higher band also moves towards the low-frequency region, but that of the lower band is also not affected.

In Figs. 5(a) and (b), it is worth noting that the changes in L_1 and L_2 hardly affect the slope of the reflected phase curve on two bands. In Fig. 5(c), as w varies from 1 to 4 mm, the slope and the width of the positive gradient reflection phase over two bands are affected together. However, the slopes of all reflected phase curves are different in both bands. Besides, the varying w also has an unbalanced effect

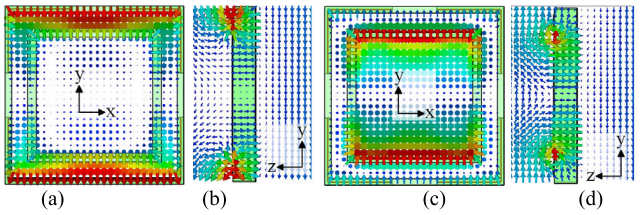

FIGURE 6. Electric field distribution of the unit cell B with $t = 0.4$ mm, $w = 2$ mm, $L_1 = 7.8$ mm, and $L_2 = 6.8$ mm is simulated in the (a) front view and (b) side view at the $f = 5$GHz. The same unit cell is also simulated in the (c) front view and (d) side view at the $f = 13$GHz.

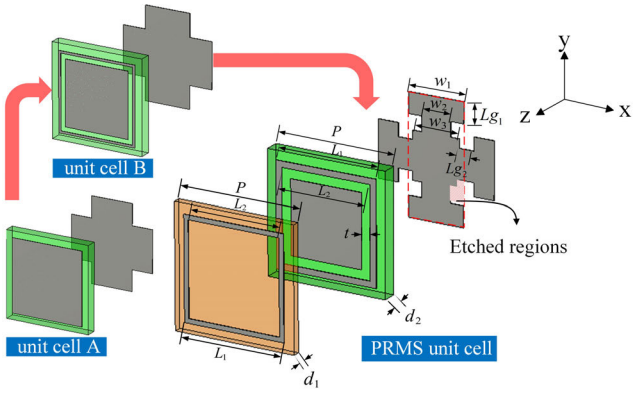

FIGURE 7. Evolution process and geometric parameters of a PRMS unit cell.

on the two bands with the positive gradient reflection phase. When w is reduced, the increase of the slope of the phase curve is more obvious in the low band than in the high band. In particular. When the width w decreases to 1 mm, the slopes k_1 and k_2 of the dual bands with positive gradient reflection phase are approximately the same. However, the unit cell B with the width w =1 mm cause a decrease in reflection magnitude, which suppresses the peak gain according to (4).

D. DESIGN of PRMS UNIT CELL

In Figs. 6(a), (b), (c), and (d), the unit cell B with $w = 2$mm, $L_1 = 7.8$mm, $L_2 = 6.8$mm and $t = 0.4$mm is simulated for the electric field distribution at 5 GHz and 13 GHz. The electric field distribution indicates that the magnetic coupling between the bottom cross patch and two square gaps of the top patch causes the positive gradient reflection phase over two bands. Therefore, we can optimize the coupling of unit cells separately to balance the slope of the positive gradient reflection phase over the two wide bands.

In order to satisfy (3) and (4), we propose two technical means to adjust the dual-band coupling and balance the dual-band slope. First of all, we differently etch two regions of the cross patch that were coupled to the top layer for a dual-wideband positive gradient reflection phase. Secondly, we press a square-ring unit cell on the unit cell B to increase the local magnetic coupling. The square-ring unit cell is composed of the top patch and a substrate with a thickness of d_1 and the permittivity of $\varepsilon_{r2} = 2.65$. The evolution process and structure of the PRMS unit cell are shown in Fig. 7.

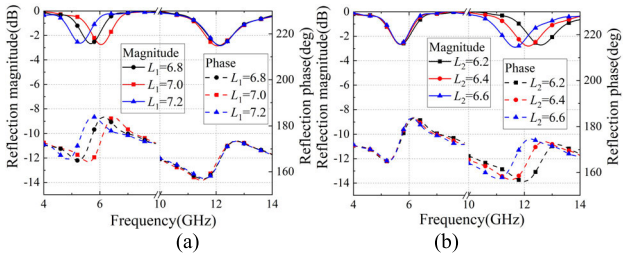

FIGURE 8. Reflection amplitude and reflection phase of PRMS unit cell. (a) $L_1 = 6.8$-7.2 mm and $L_2 = 6.4$ mm, while other structural parameters are shown in Table 1. (b) $L_1 = 7$ mm and $L_2 = 6.2$-6.6 mm, while other structural parameters are shown in Table 1.

TABLE 1. Geometric parameters of the PRMS unit cell (mm).

P	8	w_2	2	d_1	0.5
L_1	7	w_3	3	d_2	1
L_2	6.4	Lg_1	1.5	t	0.3
w_1	4	Lg_2	1		

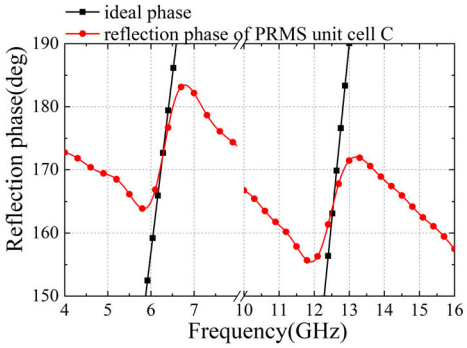

FIGURE 9. Comparison of reflection phase curves of the PRMS unit cell C and that of the ideal FP resonance condition.

Under the same boundary conditions and illumination, the PRMS unit cell with varying L_1 and L_2 is simulated for the reflection coefficient, as shown in Figs. 8(a) and (b). As the parameters changes, the PRMS unit cell produces positive gradient reflection phase over two wide bands, while the reflection amplitudes in both bands are kept above -3 dB. In Figs. 8(a) and (b), it is noted that the slopes of the two wide bands with the positive gradient reflection phase are almost the same, which is in good agreement with (3) and (4).

Besides, the changes in L_1 and L_2 can independently affect the lower and higher bands without changing the slope. To determine parameters of the PRMS unit cell and the cavity height h of the FPCA, two center frequencies of the dual-wideband high-gain radiation are fixed to 6 GHz and 12.4 GHz, as shown in Table 1. In Fig. 9, the simulated reflection phase of the PRMS unit cell in Table 1 is compared with the ideal reflection phase ϕ_H of (1). The ideal reflection phase curve agrees well with the simulated curves of the PRMS unit cell over two bands of 5.9-6.4GHz and 12.3-12.7GHz. Therefore, the PRMS consisting of the above unit cells can achieve a dual-wideband high-gain FPCA.

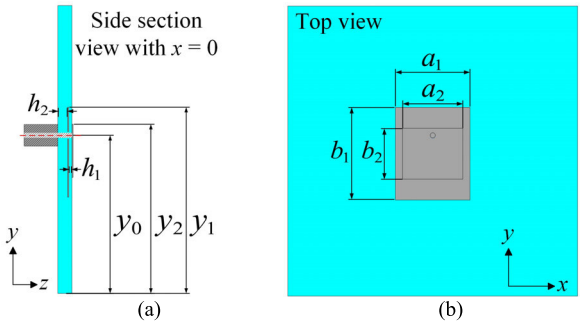

FIGURE 10. (a) side section view and (b) top view of the dual-band microstrip antenna.

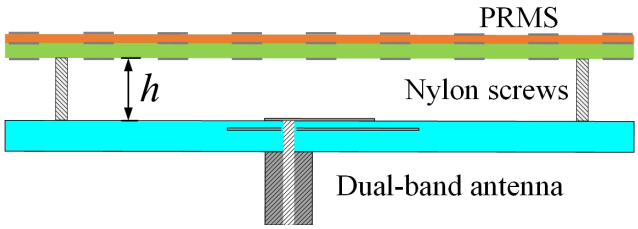

FIGURE 11. Side section view of the dual-wideband high-gain FPCA.

III. EXPERIMENTAL RESULTS

A. FEEDING ANTENNA AND FP CAVITY

To excite the dual-wideband FPCA, a normal dual-band microstrip antenna is designed as shown in Figs. 10(a) and (b). Two rectangular patches are separated by a substrate with the height of $h_1 = 0.5$ mm. The bottom patch is also spaced from the floor by another substrate with the height of $h_2 = 0.5$ mm, which is connected to the feeding coaxial line. The permittivities of two substrates are both $\varepsilon_{r3} = 2.2$. The dual-wideband FPCA is constructed by loading the PRMS of 9×9 unit cells above the dual-band microstrip antenna, as shown in Fig. 11. It is worth noting that the distance between the microstrip antenna and the PRMS, that is, the height of the FP cavity h, is very sensitive to the radiation effect. The E-plane gains of the FPCA with different h is simulated. In Figs. 12(a) and (b), the gains of the antenna with different h fluctuate over both wide bands. According to the simulated results, the designed FPCA has wider and flatter 3dB gain bandwidths in the two wide bands, when the cavity height is $h = 22.8$mm. Furthermore, according to the simulation results in Figs. 12(a) and (b), the FPCA can obtain peak gains of 12.5 dBi and 13.6 dBi and 3-dB gain bandwidths of 20.2% and 10.5% in two bands, respectively.

B. EXPERIMENTAL RESULTS AND ANALYSIS

To verify the simulation results, an FPCA prototype is fabricated for experimental measurements, as shown in Fig. 13. The aperture size and the profile height of the FPCA prototype are 1.44 λ×1.44 λ (6 GHz) / 2.96 λ × 2.96 λ (12.4 GHz) and 0.456 λ (6 GHz)/ 0.975 λ (12.4 GHz). In a microwave anechoic chamber, the FPCA prototype is measured for the reflection coefficient and peak gains in

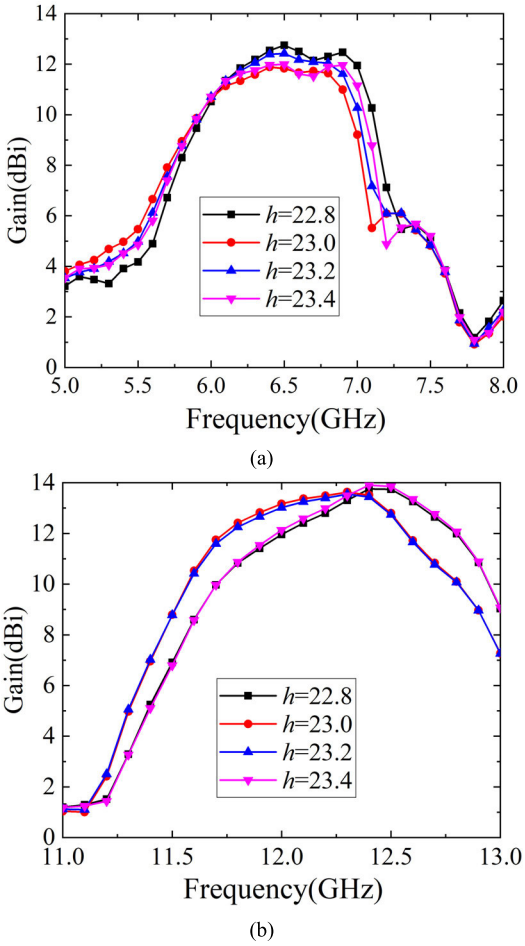

FIGURE 12. Simulated E-plane gains of the FP cavity antenna for different h at (a) 5-8GHz and (b)11-13GHz.

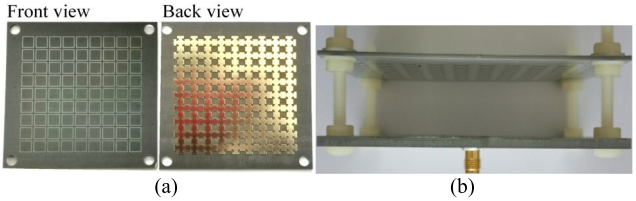

FIGURE 13. Photograph of the proposed (a) PRMS and a fabricated (b) FPCA.

E-plane and H-plane with a network analyzer. According to the calculated and measured S-parameters in Fig. 14(a), the impedance bandwidths in the two bands are 16.6% and 17.8%, respectively. The measured E-plane and H-plane gains are shown in Figs. 14(b) and (c). The measured results have good agreements with the simulated data. It can be seen that the FPCA prototype produces flat high-gain radiation over two wide bands of 5.7-6.9 GHz and 11.7-12.95 GHz. In more detail, the fabricated FPCA obtains the 3-dB gain bandwidths of 20.7% and 10.1% with peak gains of 12.07 dBi and 13.5dBi, respectively. The E-plane and H-plane patterns of peak gains in two wide bands are measured, as shown in Figs. 15 (a), (b), (c), and (d). There is a good agreement

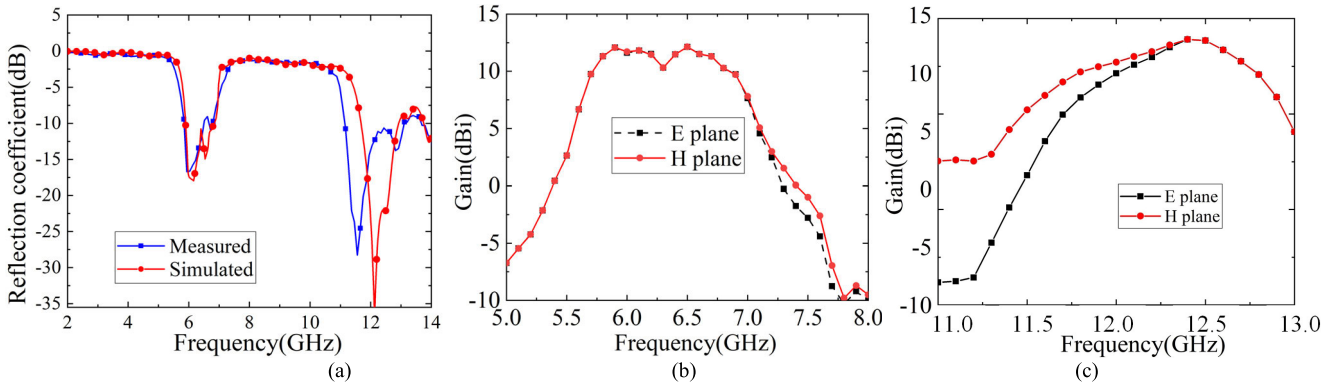

FIGURE 14. (a) Measured reflection coefficient and E-plane and H-plane gains of the FPCA prototype at (b) lower and (c) higher wide bands.

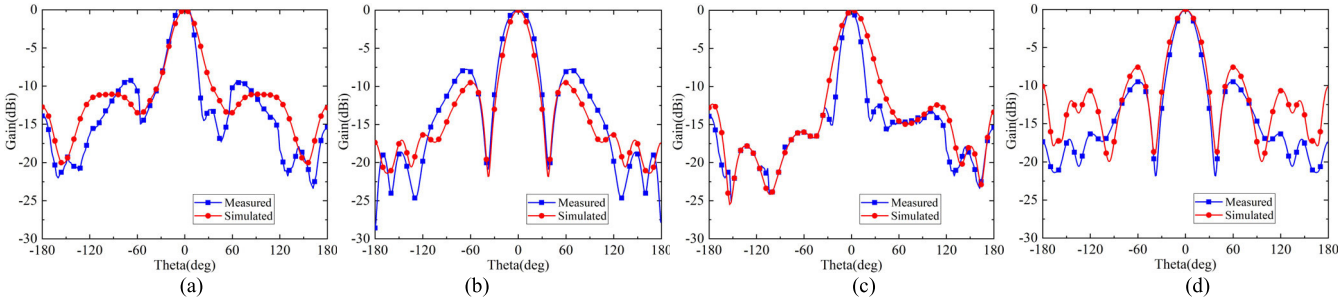

FIGURE 15. Measured E-plane patterns of the FPCA prototype at (a) 6.5GHz and (b) 12.4GHz, and H-plane patterns at (c) 6.5GHz and (d) 12.4GHz.

TABLE 2. Comparison between the proposed design and previous works.

Reference	3-dB Bandwidth		Gain(dBi)		Size(λ^2)		ε_{ap}		Profile height(λ)	
	Band 1	Band 2	Band 1	Band 2	Band 1	Band 2	Band 1	Band 2	Band 1	Band 2
[17]	4.5%	4.6%	14.5	15	5.3×5.3	6.6×6.6	4.1	2.7	0.513	0.595
[19]	7%	11%	14.9	14	1.3×1.3	3.0×3.0	70.1	12.4	0.426	0.97
[20]	4.5%	2.4%	16.2	18.5	5.31×5.31	8.0×8.0	4.6	2.3	0.499	0.751
[21]	1.41%	3.35%	16.5	20.9	2.42×2.42	4.77×4.77	22.4	7.3	0.557	1.042
[23]	4.1%	2.7%	10.1	15.2	1.49×1.49	2.67×2.67	36.2	16.9	0.345	0.617
Proposed	20.7%	10.1%	12.07	13.5	1.56×1.56	2.97×2.97	39.4	12.2	0.494	0.942

between the measured and simulated patterns on both the E-plane and H-plane. All the patterns are symmetric broadside radiation and have sidelobe levels lower than -10 dB. In Table 2, the previous works on dual-band FPCA are compared with our dual-wideband FPCA in 3-dB bandwidths, peak gains and structural characteristics. In the last two columns of Table 2, we introduce the aperture efficiency ε_{ap} to compare the radiation efficiencies, which is defined as the ratio of the radiation gain to the aperture size.

IV. CONCLUSION

To conclude, this paper innovatively proposes, designs, fabricates, and measures a dual-wideband high-gain FPCA, which achieves 3-dB bandwidths of 20.7% and 10.1% over two wide bands of 5.7-6.9 GHz and 11.7 -12.95 GHz with a single cavity, respectively. From the FP resonance condition, the technical challenges to implement dual-wideband high-gain FPCA were analyzed. By the proposed isotropic unit cell, the PRMS can provide the positive gradient reflection phase with the same slope and maintain the reflection magnitude close to 1 over two wide bands. Subsequently, a two-layer microstrip antenna is also developed as the excitation source for the dual-wideband FPCA. Finally, the fabricated prototype is measured in the microwave anechoic chamber. The measured results are in good agreement with the simulation results. In addition, the previous five related works were compared with the FPCA in this paper to demonstrate the enhanced performance of our design.

REFERENCES

[1] J. S. Turner, "New directions in communications," *IEEE J. Sel. Areas Commun.*, vol. 13, no. 1, pp. 11–23, Jan. 1995.

[2] P. Grajek, B. Schoenlinner, and G. Rebeiz, "A 24-GHz high–gain Yagi-Uda antenna array," *IEEE Trans. Antennas Propag.*, vol. 52, no. 5, pp. 1257–1261, May 2004.

[3] I. Aghanejad, H. Abiri, and A. Yahaghi, "Design of high–gain lens antenna by gradient–index metamaterials using transformation optics," *IEEE Trans. Antennas Propag.*, vol. 60, no. 9, pp. 4074–4081, Sep. 2012.

[4] F. Casares-Miranda, C. Camacho-Penalosa, and C. Caloz, "High–gain active composite right/left–handed leaky–wave antenna," *IEEE Trans. Antennas Propag.*, vol. 54, no. 8, pp. 2292–2300, Aug. 2006.

[5] G. Trentini, "Partially reflecting sheet arrays," *IRE Trans. Antennas Propag.*, vol. 4, no. 4, pp. 666–671, Oct. 1956.
[6] S. A. Hosseini, F. Capolino, and F. De Flaviis, "Single-feed highly-directive Fabry–Pérot cavity antenna for 60 GHz wireless systems: Design and fabrication," in *Proc. IEEE Antennas Propag. Soc. Int. Symp.*, Toronto, ON, Canada, Jul. 2010, pp. 1–4.
[7] D. Kim, J. Ju, and J. Choi, "A mobile communication base station antenna using a genetic algorithm based Fabry–Pérot resonance optimization," *IEEE Trans. Antennas Propag.*, vol. 60, no. 2, pp. 1053–1058, Feb. 2012.
[8] S. Franson and R. Ziolkowski, "Gigabit per second data transfer in high–gain metamaterial structures at 60 GHz," *IEEE Trans. Antennas Propag.*, vol. 57, no. 10, pp. 2913–2925, Oct. 2009.
[9] C. Chen, B. Zhang, and K. Huang, "Nonuniform Fabry–Pérot leaky–wave antenna with flat–topped radiation patterns for microwave wireless power transmission," *IEEE Antennas Wireless Propag. Lett.*, vol. 18, no. 9, pp. 1863–1867, Sep. 2019.
[10] N. Hussain, M.-J. Jeong, J. Park, and N. Kim, "A broadband circularly polarized Fabry–Pérot resonant antenna using a single–layered PRS for 5G MIMO applications," *IEEE Access*, vol. 7, pp. 42897–42907, 2019.
[11] L. Zhang, X. Wan, S. Liu, J. Y. Yin, Q. Zhang, H. T. Wu, and T. J. Cui, "Realization of low scattering for a high–gain Fabry–Pérot antenna using coding metasurface," *IEEE Trans. Antennas Propag.*, vol. 65, no. 7, pp. 3374–3383, Jul. 2017.
[12] R. Gardelli, M. Albani, and F. Capolino, "Array thinning by using antennas in a Fabry–Pérot cavity for gain enhancement," *IEEE Trans. Antennas Propag.*, vol. 54, no. 7, pp. 1979–1990, Jul. 2006.
[13] L. Zhou, X. Chen, and X. Duan, "Fabry–Pérot resonator antenna with high aperture efficiency using a double–layer nonuniform superstrate," *IEEE Trans. Antennas Propag.*, vol. 66, no. 4, pp. 2061–2066, Apr. 2018.
[14] Y. Ge, K. P. Esselle, and T. S. Bird, "The use of simple thin partially reflective surfaces with positive reflection phase gradients to design wideband, low–profile EBG resonator antennas," *IEEE Trans. Antennas Propag.*, vol. 60, no. 2, pp. 743–750, Feb. 2012.
[15] K. Konstantinidis, A. P. Feresidis, and P. S. Hall, "Multilayer partially reflective surfaces for broadband Fabry–Pérot cavity antennas," *IEEE Trans. Antennas Propag.*, vol. 62, no. 7, pp. 3474–3481, Jul. 2014.
[16] P.-Y. Qin, L.-Y. Ji, S.-L. Chen, and Y. J. Guo, "Dual–polarized wideband Fabry–Pérot antenna with quad–layer partially reflective surface," *IEEE Trans. Antennas Propag.*, vol. 17, no. 4, pp. 551–554, Apr. 2018.
[17] P. Xie, G. Wang, X. Kong, and J. Li, "Design of a novel metasurface for dual-band Fabry–Pérot cavity antenna," *Int. J. RF Microw. Comput.-Aided Eng.*, vol. 28, no. 2, 2018, Art. no. e21181.
[18] F. Qin, S. Gao, Q. Luo, G. Wei, J. Xu, J. Li, C. Wu, C. Gu, and C. Mao, "A triband low–profile high–gain planar antenna using Fabry–Pérot cavity," *IEEE Trans. Antennas Propag.*, vol. 65, no. 5, pp. 2683–2688, May 2017.
[19] M. L. Abdelghani, H. Attia, and T. A. Denidni, "Dual- and wide-band Fabry–Pérot resonator antenna for WLAN applications," *IEEE Antennas Wireless Propag. Lett.*, vol. 16, pp. 473–476, 2016.
[20] E. B. Lima, J. R. Costa, and C. A. Fernandes, "Multiple–beam focal–plane dual–band Fabry–Pérot cavity antenna with reduced beam degradation," *IEEE Trans. Antennas Propag.*, vol. 67, no. 7, pp. 4348–4356, Jul. 2019.
[21] F. Meng and S. K. Sharma, "A dual–band high–gain resonant cavity antenna with a single layer superstrate," *IEEE Trans. Antennas Propag.*, vol. 63, no. 5, pp. 2320–2325, May 2015.
[22] H. Klaina, B. Ratni, A. V. Alejos, O. Aghzout, and S. N. Burokur, "Directive dual-band Fabry–Pérot cavity antenna for 5G-IoT near-ground communications," in *Proc. 13th Eur. Conf. Antennas Propag. (EuCAP)*, Mar. 2019.
[23] J. Chen, Y. Zhao, Y. Ge, and L. Xing, "Dual-band high-gain Fabry–Pérot cavity antenna with a shared-aperture FSS layer," *IET Microw., Antennas Propag.*, vol. 12, no. 13, pp. 2007–2011, Oct. 2018.

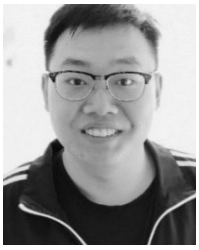

YAN-HE LV (Student Member, IEEE) was born in Heilongjiang, China, in 1995. He received the B.E. degree from the Institute of Applied Physics, University of Electronic Science and Technology of China, Chengdu, China, in 2017, where he is currently pursuing the Ph.D. degree in radio physics. His current research interests include metasurface, antenna theory, and computational electromagnetics.

XIAO DING (Member, IEEE) received the Ph.D. degree in radio physics from the University of Electronic Science and Technology of China (UESTC), Chengdu, China, in 2013. In 2013, he joined the Department of Electrical and Computer Engineering, South Dakota School of Mines and Technology, Rapid City, SD, USA, as a Research Scholar. In 2014, he joined UESTC, where he is currently an Associate Professor. From 2016 to 2017, he was a Visiting Scholar with the Applied Electromagnetics Laboratory, University of Houston, Houston, TX, USA. His current research interests include antenna theory and computational electromagnetics.

BING-ZHONG WANG (Senior Member, IEEE) received the Ph.D. degree in electronic engineering from the University of Electronic Science and Technology of China (UESTC), Chengdu, in 1988.

He joined UESTC, in 1984, where he is currently a Professor. He has been a Visiting Scholar with the University of Wisconsin–Milwaukee, WI, USA, a Research Fellow with the City University of Hong Kong, Hong Kong, and a Visiting Professor with the Electromagnetic Communication Laboratory, Pennsylvania State University, University Park, PA, USA. He has authored or coauthored over 200 technical publications and authored three books. His current research interests include computational electromagnetics, antenna theory and techniques, and time-reversed electromagnetics.

Dr. Wang was a four-time recipient of the Second-Class Science and Technology Progress Prizes by the Ministry of Education of China and the Sichuan Province Government, China. He also received awards from the Trans-Century Foundation for Talents from the Ministry of Education of China and Fok Ying-Tong Education Foundation. He serves as the Vice President of the Microwave Society of the Chinese Institute of Electronics and the Chair of the IEEE MTT Chengdu Chapter.